Rupture and frequency-dependent seismic radiation of the 2012 $M_{\rm w}$ 8.6 Sumatra strike-slip earthquake

Jiuxun Yin[1,2] and Huajian Yao[1,2]

[1]*Laboratory of Seismology and Physics of Earth's Interior, School of Earth and Space Sciences, University of Science and Technology of China, Hefei, Anhui 230026, China*
[2]*National Geophysical Observatory at Mengcheng, Anhui, China. E-mail: hjyao@ustc.edu.cn*

SUMMARY

On 2012 April 11, a great strike-slip earthquake (moment magnitude of $M_{\rm w}$ 8.6) occurred off the west coast of northern Sumatra area followed by an $M_{\rm w}$ 8.2 aftershock 2 hr later. Different geophysical data and methods have been used to investigate the mechanism, faulting, seismic radiation and slip propagation of this event, but frequency-dependent features of its rupture process have not been discussed much. In this study, we use a compressive sensing method based on sparsity inversion in the frequency domain to study the frequency-dependent seismic radiation and rupture process of this event. Our results indicate a very complex rupture process concerning at least three different rupture stages on multiple subfaults with nearly conjugate geometries. The main shock has triggered seismicity on a series of ridge-perpendicular or ridge-parallel conjugate strike-slip faults around the Nighty East Ridge. Obvious frequency-dependent rupture process has been presented and discussed. Combining results from slip inversion based on the finite-fault model, we observe that in the beginning stage of the rupture lower frequency radiation appears to originate from the areas with large slip, while the high-frequency radiation is located at the boundary of large-slip region or rupture front. Some radiation probably originates from the repeating slip on the main faults or triggered events on some nearby faults in the rupture area. The complex frequency-dependent seismic radiation patterns observed in this study provide important information for future investigation of rupture physics of this complex strike-slip event.

Key words: Inverse theory; Earthquake source observations; Intra-plate processes; Fractures and faults; Indian Ocean.

1 INTRODUCTION

In the history of instrumental seismology, great strike-slip earthquakes with magnitudes close to 8 or above are not very common. Since the 21st century, the 2001 Kunlunshan $M_{\rm w}$ 7.8 event, the 2002 Denali $M_{\rm w}$ 7.9 event and the 2004 Macquarie Island $M_{\rm w}$ 8.1 event offer us good examples to study large strike-slip earthquakes (Tsuboi *et al.* 2003; Hayes *et al.* 2009). However, great strike-slip earthquakes are usually complicated in seismogenic models and rupture processes. Prior assumptions of source parameters may have significant effects on results of slip history even for a relatively simple unilateral event (Tocheport *et al.* 2006). And super-shear rupture phenomenon appears to occur for some of the great strike-slip earthquakes such as the 1999 Izmit, 2001 Kunlunshan and 2002 Denali earthquakes (Bouchon *et al.* 2001; Bouchon & Vallée 2003; Walker & Shearer 2009).

On 2012 April 11, a great intraplate strike-slip earthquake of $M_{\rm w}$ 8.6 occurred off the west coast of northern Sumatra and was followed by an $M_{\rm w}$ 8.2 great aftershock 2 hr later (see Fig. 1, focal

mechanisms in orange). The Sumatra subduction region is well-known for its high seismicity rate, occurrence of great earthquakes as well as tsunami risks. However, most earthquakes occurred at the plate boundary between the Indo-Australia Plate and Sunda Plate with thrusting mechanisms. For intraplate earthquakes outside the Sumatra subduction zones, a majority of them are expressed as normal faulting. This $M_{\rm w}$ 8.6 intraplate strike-slip event west of the Sumatra subduction zone is very unusual and attracts lots of attention (e.g. Duputel *et al.* 2012; Meng *et al.* 2012; Satriano *et al.* 2012; Yue *et al.* 2012; Ishii *et al.* 2013; Wei *et al.* 2013). This event is probably caused by the oblique plate convergence (see Fig. 1, black arrow) with sufficient trench-parallel strain accumulation since the last megathrust event (Ishii *et al.* 2013). This great strike-slip earthquake has also caused a fivefold increase of far remote earthquake occurrence 6 d after the main shock (Pollitz *et al.* 2012). Interestingly, there was an $M_{\rm w}$ 7.2 earthquake (Fig. 1, the blue beach ball) occurred on 2012 January 10 nearly at the same location of the main $M_{\rm w}$ 8.6 earthquake. This smaller event has a similar focal mechanism as the $M_{\rm w}$ 8.6 one and can be
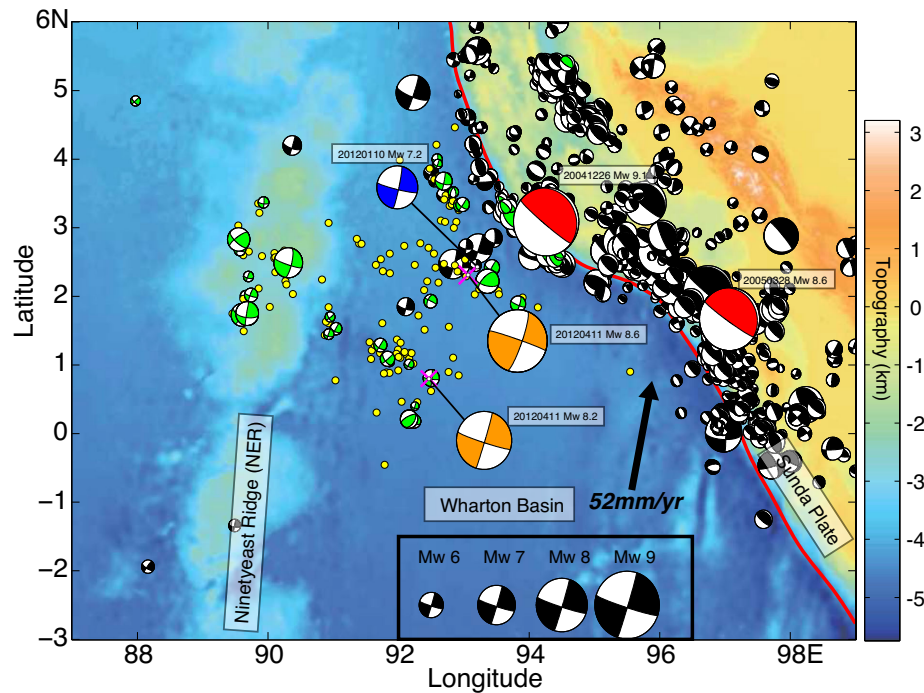
Figure 1. Earthquake locations and focal mechanisms in the Sumatra area. The 2012 April 11 M_w 8.6 event and its M_w 8.2 aftershock are shown as the orange beach balls, the 2012 M_w 7.2 foreshock is shown as blue, and the beach balls in green are other large aftershocks. Three beach balls (in blue and orange) are connected with their epicentres by thin black lines. The 2004 M_w 9.1 and 2005 M_w 8.6 megathrust events are shown as the red beach balls. The beach balls in black show large earthquakes that occurred in the past 10 yr before the 2012 M_w 8.6 event. All focal mechanisms are from GCMT (http://www.globalcmt.org). The purple crosses show the epicentres of the 2012 M_w 8.6 and M_w 8.2 event and the yellow circles are the aftershocks with magnitude ≥ 4 within the first 2 d after the M_w 8.6 main shock (from the U.S. Geological Survey (USGS), http://earthquake.usgs.gov/earthquakes/). Background image shows the topography from the ETOPO1 global relief model (http://www.ngdc.noaa.gov/mgg/global/global.html). The black arrow indicates the direction of convergence ($\sim$52 mm yr^{-1}) of Indo-Australia with respect to the Sunda Plate. Red line shows the trench line of the Sumatra subduction zone.

used as the calibration event to study the main shock (Wei *et al.* 2013).

Several different methods have been applied to investigate this M_w 8.6 earthquake including inversion of multiple source parameters (Duputel *et al.* 2012), slip inversion (Yue *et al.* 2012; Wei *et al.* 2013) and high-frequency seismic radiation from backprojection (Meng *et al.* 2012; Satriano *et al.* 2012; Wang *et al.* 2012; Ishii *et al.* 2013). These studies have revealed that this strike-slip event is remarkably complex for its rupture process because of the large-scale rupture area, long duration of rupture (about 170 s) and the complexity of the source region. Wang *et al.* (2012) found this event exhibits supershear rupture feature from backprojection analysis.

Although Satriano *et al.* (2012) show quite different seismic radiation patterns of this Sumatra event in the 0.1–0.5 Hz and 0.5–1.0 Hz, previous studies did not discuss much about the frequency-dependent rupture process of this strike-slip event. The occurrence of the M_w 9.0 Tohoku earthquake in 2011 aroused lots of attention in the community of seismology due to its frequency-dependent rupture characteristics. Earlier studies of the Tohoku event discovered that the regions of high-frequency radiation do not overlap with the area with large coseismic slip (Simons *et al.* 2011; Wang & Mori 2011; Lay *et al.* 2012). To understand the physics of this phenomenon, Yao *et al.* (2011, 2013) proposed to use the compressive sensing (CS) method, which is originated from the community of signal processing and applied mathematics (Candes *et al.* 2006; Donoho 2006), to invert for the sparse distribution of frequency-dependent seismic radiation during large earthquake rupture. The radiated high-frequency seismic energy is usually associated with sudden changes of rupture or slip behaviour from previous theo-

retical and numerical studies (Yamashita 1983; Spudich & Frazer 1984; Sato 1994), for instance, sudden changes of rupture speed or rupture direction due to variations of frictional properties at the fault surface. Therefore, the regions that radiate high-frequency seismic energy are sparse in space, which leads to the utilization of the CS method for studying seismic radiation during earthquake rupture. However, some other rupture properties, such as the accumulated slip, are not sparse in space.

In this paper, we use the CS method and the Hi-net array (High Sensitivity Seismograph Network; Obara *et al.* 2005) data in Japan to investigate the seismic radiation and rupture process of the great strike-slip earthquake (M_w 8.6) off the west coast of Sumatra on 2012 April 11. In order to make the inversion procedure more stable and more resistant to outliers in the data, we introduce a different minimization scheme in the inversion than that was used in Yao *et al.* (2011). We will show frequency-dependent features of seismic radiation of this earthquake, compare seismic radiation patterns with the slip inversion results and discuss its complex rupture processes.

2 DATA

To investigate this 2012 April 11 Sumatra earthquake, we use the first 170 s teleseismic *P*-wave data (velocity seismograms) from dense Hi-net stations in Japan after removing the mean, trend and instrumental responses, resampling to 10 Hz sampling rate, and bandpass filtering in the frequency band 0.05–4 Hz.

We perform some pre-processing for the array data in order to select high quality waveforms and suppress effects from 3-D structural heterogeneities. First, we calculate the signal-to-noise
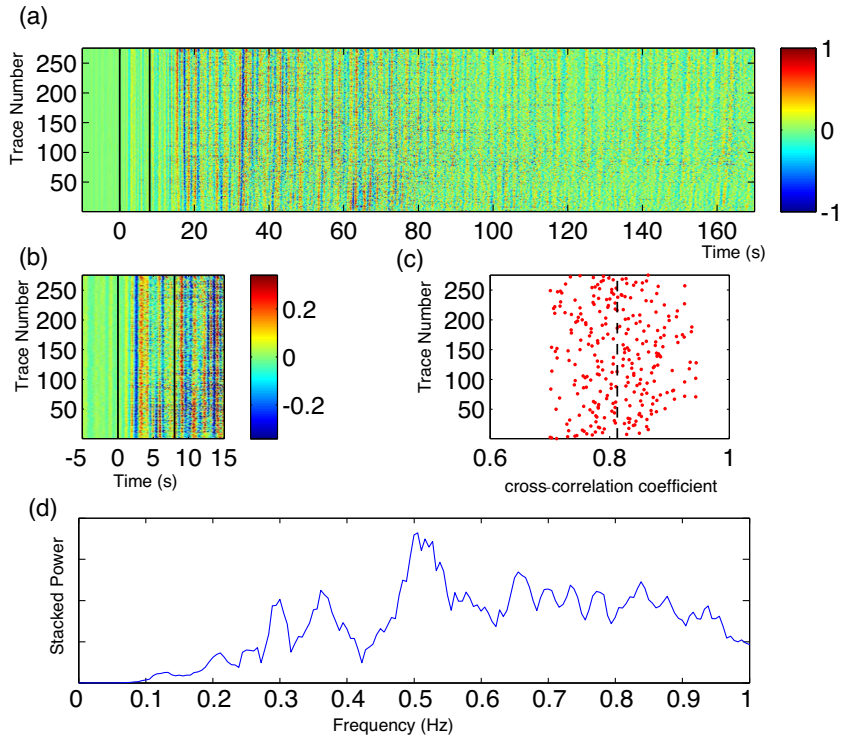
Figure 2. Teleseismic *P* waves recorded by the Hi-net stations (see Fig. 3) in the frequency band 0.05–4 Hz used in this study. (a) Aligned waveforms from the selected 275 stations in Fig. 3. Waveforms between the two black lines (at the time 0 and 8 s) are used for the cross-correlation analysis to align the waveforms iteratively. The time at 0 s indicates the beginning of the P phase. (b) Zoom-in of the waveforms from –5 to 15 s in (a). (c) Cross-correlation coefficients between the waveform within the time window [0 8] s of each station and their reference stack (see texts in the Data section for the detail). Only stations with SNR > 15 and cross-correlation coefficient > 0.7 are shown here. Dashed line presents the average cross-correlation coefficient of all the selected stations. (d) Stacked energy spectrum of all selected waveforms in (a).

ratio (SNR) of the *P* waves for each station and only keep the stations with SNR > 15 to assure the data quality. Then we use a multichannel cross-correlation method (VanDecar & Crosson 1990; Ishii *et al.* 2005) to align the *P* waves. We stack the waveforms of all stations (see Fig. 2) to generate a reference stack, cross-correlate the initial 8 s *P* waves of each station with the reference stack to correct the time-shift and compute the cross-correlation coefficient for each station. Then seismograms with cross-correlation coefficients above 0.7 are used to generate the next-generation reference stack. These steps are repeated for several times and finally we only keep the aligned waveforms with correlation coefficients above 0.7 with respect to the reference stack (Fig. 2c, also see Fig. S1 for the detailed information of station selection).

Waveforms from 275 stations (Fig. 3) satisfy our data pre-processing requirements and are used to study the rupture process of this earthquake. We also analyse the spectrum information of the first 170 s teleseismic *P* waves by stacking the power spectrum of each station (Fig. 2d). The stacked power spectrum concentrates at higher frequencies above 0.2 Hz and the peak is at about 0.5 Hz. The sharp decrease of the observed lower frequency energy (less than 0.3 Hz) is mainly due to the bandwidth limit of the Hi-net stations, which have the corner frequency around 1 Hz (Obara *et al.* 2005).

3 METHODOLOGY

In this section, we will present the methodology of CS that is used for studying seismic radiation during earthquake rupture using tele-seismic *P* waves. A series of synthetic tests are designed to assure the feasibility of this method and the reliability of its results. Since

teleseismic *P* waves have nearly vertical outgoing rays in the source region for shallow earthquakes, we typically investigate the rupture process projected on the horizontal plane at the focal depth due to the lack of depth resolution. We refer to this plane as the projected rupture plane throughout the text.

3.1 Compressive sensing and beamforming of earthquake rupture

For the predefined grids on the projected rupture plane, the spatio-temporal distribution of rupture process can be expressed by a vector of source time functions to be solved:

$$\mathbf{x}(t) = [x_1(t), x_2(t), x_3(t), \ldots, x_M(t)]^T \tag{1}$$

in which *M* is the number of gridpoints and each element of **x** represents an individual source time function at each gridpoint. The teleseismic *P* waves recorded by the array stations can be expressed by a vector of time-series:

$$\mathbf{b}(t) = [b_1(t), b_2(t), b_3(t), \ldots b_N(t)]^T \tag{2}$$

in which *N* is the number of stations. Here we use teleseismic ve-locity seismograms, which are proportional to the slip acceleration in the source area.

In order to obtain the temporal distribution of rupture process, we apply a sliding time window scheme to the aligned *P* waves in Fig. 2 (Yao *et al.* 2011). We transform the observed data in each time window to the frequency domain using the Fourier transformation and therefore obtain the observed data spectra

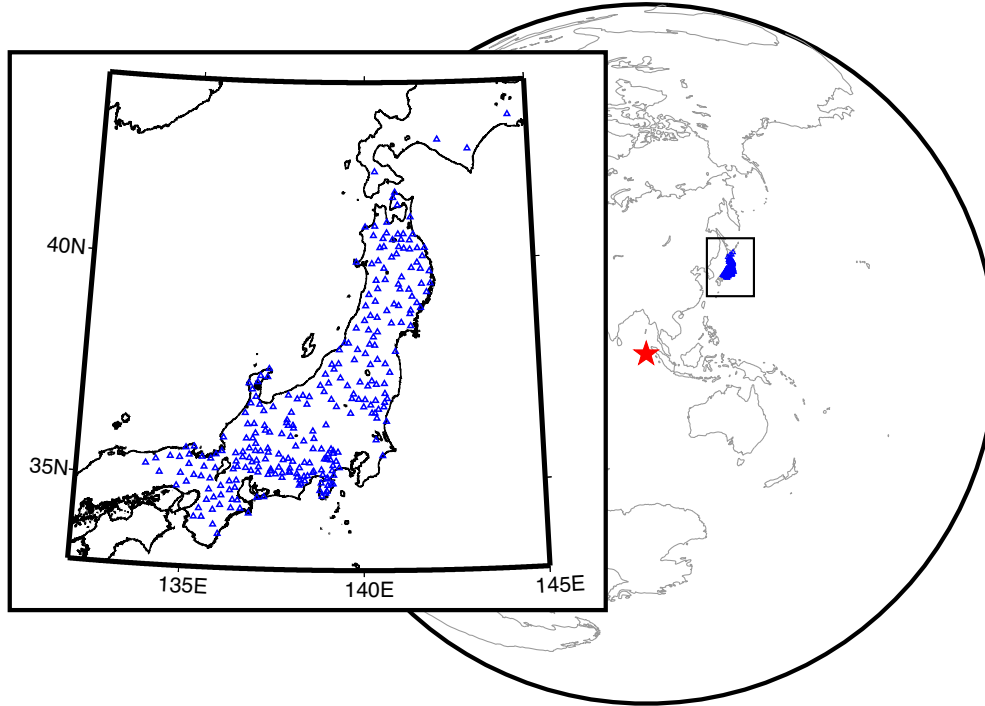$$\mathbf{B}(\omega) = [B_1(\omega), B_2(\omega), B_3(\omega), \ldots B_N(\omega)]^T. \tag{3}$$

Figure 3. Epicentre of the 2012 April 11 M_w 8.6 earthquake in Sumatra (red star) and the selected 275 Japanese Hi-net stations (blue triangles) used in this study (see Fig. 2, Fig. S1 and Data section for the criteria of station selection).

And the source time vector $\mathbf{x}(t)$ in the given time window can be similarly transformed into the frequency domain to obtain the source spectra:

$$\mathbf{X}(\omega) = [X_1(\omega), X_2(\omega), X_3(\omega), \dots, X_M(\omega)]^T. \tag{4}$$

The link between the observed data $\mathbf{B}(\omega)$ and $\mathbf{X}(\omega)$ is the frequency-domain $N \times M$ transmission (or phase spectrum) matrix $\mathbf{A}(\omega)$ whose entries are

$$A_{nm} = e^{-i\omega(\tau_{nm}-t_{n0})} \tag{5}$$

in which τ_{nm} is the traveltime from the mth gridpoint to the nth station and t_{n0} is the predicted traveltime from the nth station to the hypocentre using a 1-D global reference model due to the alignment of the P waves (Yao *et al.* 2011). A_{nm} represents the phase difference in the frequency domain that comes from the traveltime difference in the time domain. Therefore, we can solve the following equation for the source spectra $\mathbf{X}(\omega)$:

$$\mathbf{B}(\omega) = \mathbf{A}(\omega)\mathbf{X}(\omega) + \mathbf{noise}(\omega), \tag{6}$$

where $\mathbf{noise}(\omega)$ is the noise vector. The equation above is typically underdetermined, that is, $M > N$.

In order to obtain the sparse distribution of seismic radiation during earthquake rupture process, Yao *et al.* (2011, 2013) proposed to use the following sparsity inversion scheme:

$$\hat{\mathbf{X}}(\omega) = \mathrm{argmin}\,[\|\mathbf{B}(\omega) - \mathbf{A}(\omega)\mathbf{X}(\omega)\|_2 + \lambda\|\mathbf{X}(\omega)\|_1], \tag{7}$$

where λ is a damping parameter. This kind of equation based on the L2 norm of the data misfit and L1 norm of the model vector (or called the L2–L1 minimization problem) can be efficiently solved by the interior point theory based on convex optimization (Boyd & Vandenberghe 2004).

Based on the inverse theory and applications (Yang & Zhang 2011; Aster *et al.* 2013), the L1 norm of data misfit is more resistant

against data outliers compared with the L2 norm of data misfit, so eq. (7) can be modified as

$$\hat{\mathbf{X}}(\omega) = \mathrm{argmin}\,[\|\mathbf{B}(\omega) - \mathbf{A}(\omega)\mathbf{X}(\omega)\|_1 + \lambda\|\mathbf{X}(\omega)\|_1]. \tag{8}$$

And the source power of the lth gridpoint from the CS method can be expressed as

$$P_l^{CS}(\omega) = |\hat{X}_l(\omega)|^2. \tag{9}$$

Yao *et al.* (2011) gave a method to estimate λ in the L2–L1 norm minimization problem of the eq. (7). For the L1–L1 norm inversion problem of the eq. (8), if there is only one source without noise, $\|\mathbf{A}(\omega)\mathbf{X}(\omega)\|_1 = N\|\mathbf{X}(\omega)\|_1 = \|\mathbf{B}(\omega)\|_1$. To balance both terms in the right-hand side of the eq. (8) in a similar scale, we have $\|\mathbf{B}(\omega) - \mathbf{A}(\omega)\mathbf{X}(\omega)\|_1 \sim \lambda\|\mathbf{X}(\omega)\|_1$. Therefore, $\lambda \sim N\frac{\|\mathbf{B}(\omega)-\mathbf{A}(\omega)\mathbf{X}(\omega)\|_1}{\|\mathbf{B}(\omega)\|_1}$, which is close to the number of stations (N) times the approximate noise-to-signal ratio of the data $[\frac{\|\mathbf{B}(\omega)-\mathbf{A}(\omega)\mathbf{X}(\omega)\|_1}{\|\mathbf{B}(\omega)\|_1}]$. From the one-source assumption we have an approximate range of damping factor λ and by using the L-curve method (Aster *et al.* 2013) we can have a better estimate of λ in the problems of multiple sources and varying noise level in the real data inversion. The most important advantage of CS method is that it has high spatial resolution and its resolution is not severely limited by the distribution (Figs S2a and d) of or the number (Figs S3b and c) of stations under the sparsity constraints, which is satisfied in our problem. Thus the CS method can deal with the source location problem with high resolution.

Beamforming is another widely used frequency-domain method to solve the eq. (6) to obtain the radiated source power on the projected rupture plane. To compare with the CS results we also apply this method in our study. The least squares solution of eq. (6) is $\tilde{\mathbf{X}} = (\mathbf{A}^H\mathbf{A})^{-1}\mathbf{A}^H\mathbf{B}$ with the superscript ^{H} denoting the matrix complex conjugate or Hermitian, and the diagonal element of $\mathbf{A}^H\mathbf{A}$
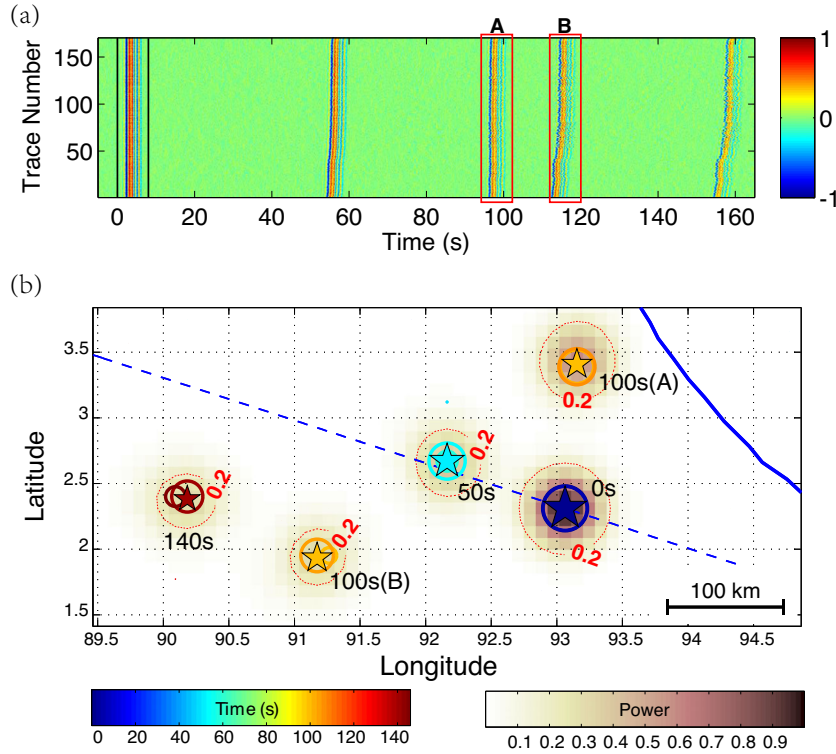
Figure 4. (a) Synthetic waveforms for the Hi-net stations (see Fig. 3) after alignment, which are produced by 5 input point sources with different amplitudes [scaled 1.0, 0.8, 0.7, 0.7, 0.6, see (b)]. Time windows A and B (red rectangles) are two sources with the same source origin time. (b) Recovered sources (coloured open circles) from the CS method using the synthetic waveforms in the frequency band between 0.2 and 1 Hz. Stars are the synthetic sources we set and the nearby numbers are the source origin times. Sources A and B have the same source origin time 100 s [waveforms shown in (a)]. Colour of each circle indicates the recovered source origin time. The background image shows the total source power from the CS method. Red dashed contours indicate 20 per cent of the maximum power. The blue dashed line shows the strike of the 2012 M_w 8.6 event (from USGS) and the blue line for the Sumatra trench location.

is N. If we approximate $\mathbf{A}^H\mathbf{A} \approx N\mathbf{I}$, $\tilde{\mathbf{X}} = \frac{1}{N}\mathbf{A}^H\mathbf{B}$, which is the adjoint solution of eq. (6). The lth element of $\tilde{\mathbf{X}}$ is:

$$(\tilde{\mathbf{X}})_l = \frac{1}{N}\sum_{p=1}^{N} e^{i\omega(\tau_{pl}-t_{p0})} B_p. \tag{10}$$

This form of solution has a clear physical meaning: we first correct the phase difference for the signal from the lth gridpoint to each station and average all the shifted spectra. This phase correction and stack can suppress the incoherent phases and random noise and enhance the coherent signal by improving the SNR about $\sqrt{N}$ times (Rost 2002). The beamforming power at the lth grid is thus $P_l^{BF}(\omega) = |\tilde{X}_l(\omega)|^2$. This method is analogous to the backprojection method in the time-domain and can also get the distribution of seismic energy radiation at certain frequency during earthquake rupture process. However, the spatial resolution of this simple aligning-and-stacking method is limited by the size of the array and distribution of array stations (Figs S2b and e). This method may give incorrect results when dealing with multi-source problems (see Section 3.2), which are very common in the earthquake events with bilateral rupture process.

The high-resolution beamforming method such as the MUSIC method (Meng *et al.* 2011) can be used to improve the resolution of traditional beamforming analysis with proper estimation of data covariance matrix. The CS method based on sparsity can achieve much higher resolution in the problems of source localization than the conventional beamforming method (Yao *et al.* 2011) as well as the high-resolution beamforming techniques (Malioutov *et al.*

2005), such as the Capon's method (Capon 1969) and the MUSIC method (Schmidt 1986), especially in the relatively lower frequency band (see Yao *et al.* 2011).

In real situation, seismic waves originating from the source closer to the array may arrive earlier than the farther source with the same or even later source time on the seismogram (see A, B in Fig. 4). When using the sliding window, we need to make proper corrections to get a right source origin time. Similar as shown in Yao *et al.* (2011), for one time window $[t_b\ t_e]$, in which t_b is the beginning time and t_e is the ending time of this time window, the source time correction is calculated as $\Delta t = \text{median}(t_{0n} - \tau_{mn})$, where t_{0n} and τ_{mn} are the traveltime from the epicentre and mth gridpoint to the nth station, respectively. The operator 'median' here takes the median value of the time-shifts for all N stations. Thus we have the corrected source time as

$$t_s = (t_b + t_e)/2 + \Delta t = (t_b + t_e)/2 + \text{median}(t_{0n} - \tau_{mn}). \tag{11}$$

Following Yao *et al.* (2011), for each snapshot (time window), source power of each frequency is smoothed using a Gaussian weight function and all the smoothed power at each frequency is summed up to obtain the total source power distribution in a frequency band at the snapshot centred at time t:

$$\hat{P}_l^{CS}(t) = \frac{C}{K}\sum_{k=1}^{K}\sum_{i=1}^{M} \exp\left\{-\frac{d_{il}^2}{R^2}\right\} P_l^{CS}(\omega_k, t). \tag{12}$$

In (12) d_{il} is the distance between ith and the lth gridpoint, C is a scaling constant, and R is smoothing distance ($R = 50$ km in this
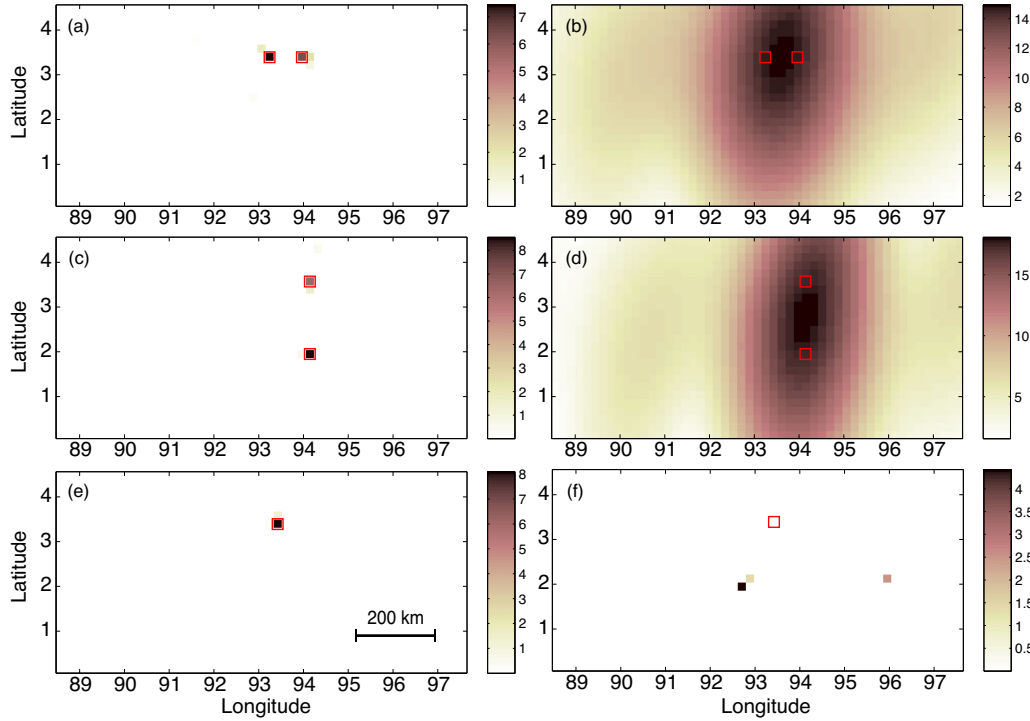
Figure 5. Results of the synthetic tests with two sources (a–d) and the outlier test with one source (e, f) from different methods: (a, c) L1–L1 norm CS results; (b, d) beamforming results; (e) L1-L1 norm CS results; (f) L2–L1 norm CS results. Red open squares are the input point sources and the background image is the source power distribution recovered from the CS or beamforming method. The data frequency is 0.5 Hz in these tests.

study). $P_l^{CS}(\omega_k, t)$ is the CS power in (9) at frequency ω_k ($k = 1$, $2, \ldots, K$, and K is the number of frequency points) and time snapshot t.

3.2 Synthetic and resolution tests

We design a series of synthetic and resolution tests to assure the robustness of our L1–L1 norm based CS method. We also compare the results from the L2–L1 norm CS method and the conventional beamforming method. In all the tests, we use the same geometry of the source grids as used in the Section 4.

We set 2 point sources with equal amplitude in the study region (red open squares in Fig. 5) and generate the observed spectra based on the IASP91 global model (Kennett & Engdahl 1991) at the frequency 0.5 Hz using eq. (6) for the same 275 Hi-net array stations shown in Fig. 3. The level of random noise is set to be 10 per cent of the input source amplitude. The L1–L1 norm based method has the ability to distinguish the spatially separated two point sources with quite good accuracy (Figs 5a and c). However, the conventional beamforming method can hardly separate the two point sources (Figs 5b and d) due to strong phase interference. Meanwhile, the results clearly show that the spatial resolution of beamforming method is influenced by the distribution of the array stations (see Figs 3 and S2b and e) and varies in different orientations. On the contrary, CS results are rarely affected.

We also use the single source model (Figs 5e and f) to test the robustness of the inversion results based on the L1–L1 and L2–L1 norm methods against data outliers. In this outlier test, we randomly select 8 stations in the data set and add random noise with amplitudes about 5 times of the input source amplitude with random phase shifts. By this means, a new data set contaminated by eight outliers

is generated and used to test our inversion method. The inversion result based on the L1–L1 norm method is very stable and accurate, which is almost not affected by the data outliers (Fig. 5e). While for the results based on the L2–L1 norm inversion, only ∼3 per cent outliers in the data will lead to large spatial shift of the inversion results (Fig. 5f). This test confirms that the L1–L1 norm based CS method has much better resistance against outliers than the L2–L1 norm based method.

To test performance of the CS method using a sliding window approach in the time domain (Yao *et al.* 2011), we design another synthetic test. The synthetic waveforms (Fig. 4a) are generated by five different (point) sources with different origin times and locations as shown in Fig. 4(b). The first 8 s stacked *P* waveform of all traces in Fig. 2(a) is used as the source wavelet to produce the aligned synthetic waveforms (with 10 per cent random noise) as shown in Fig. 4(a). After applying the CS method using a 10-s long sliding window for the aligned waveforms (Fig. 4a), we get the spatial and temporal distribution of sources in the frequency band between 0.2 and 1 Hz as shown in Fig. 4(b). Not only the positions but also the source origin times have been well recovered from our method even for the two sources with the same starting time. This test results indicate that our inversion procedure for the coseismic subevent distribution in space and time is quite accurate using the sliding window approach.

4 RESULTS

4.1 Results at different frequencies

Since the CS inversion method can more accurately locate the source position at different frequencies, we show the spatial and temporal
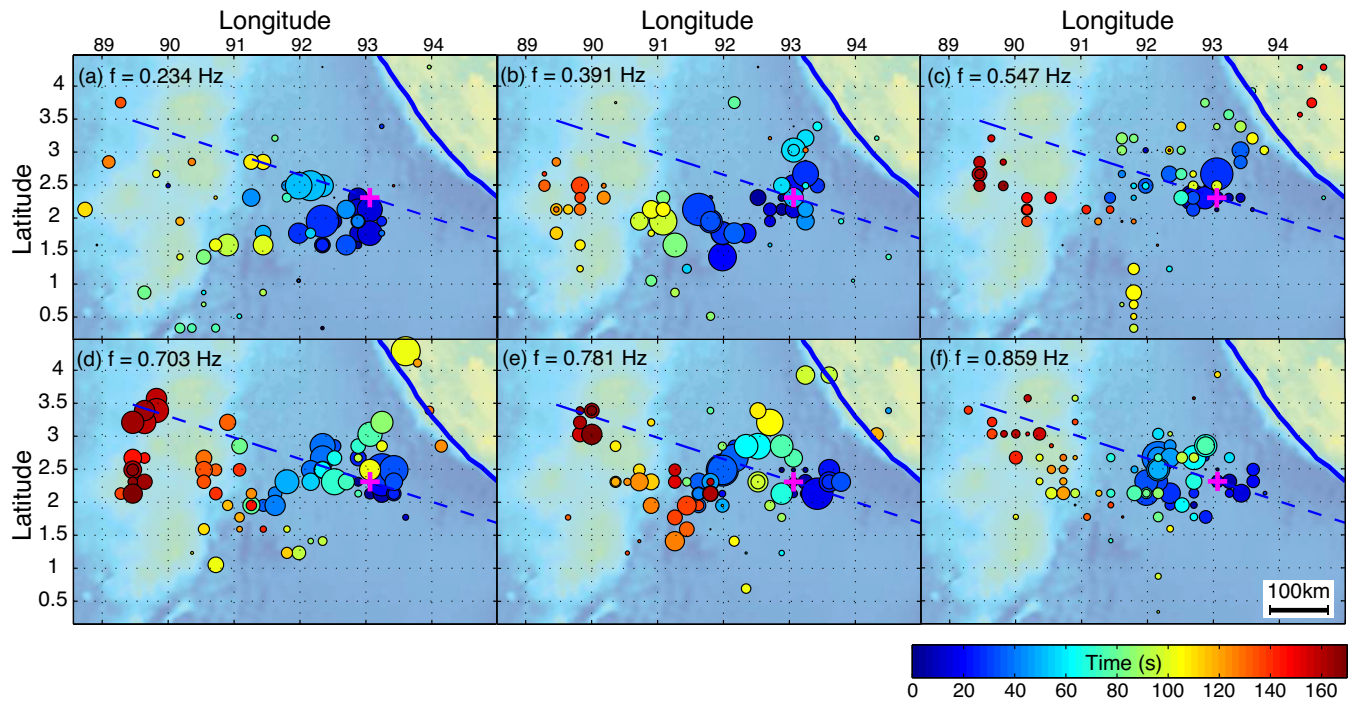
Figure 6. Coseismic sources distribution of the 2012 Sumatra M_w 8.6 earthquake from the CS method at 6 different frequencies: (a) 0.234 Hz, (b) 0.391 Hz, (c) 0.547 Hz, (d) 0.703 Hz, (e) 0.781 Hz and (f) 0.859 Hz. Coloured circles are the coseismic sources inverted from different time windows with the right colourbar giving the source origin time. The area of each circle is proportional to the source power (normalized separately for each frequency). The purple cross gives the epicentre of the main shock from USGS (2.311°N, 93.063°E). Blue and dashed lines are the same as in Fig. 4.
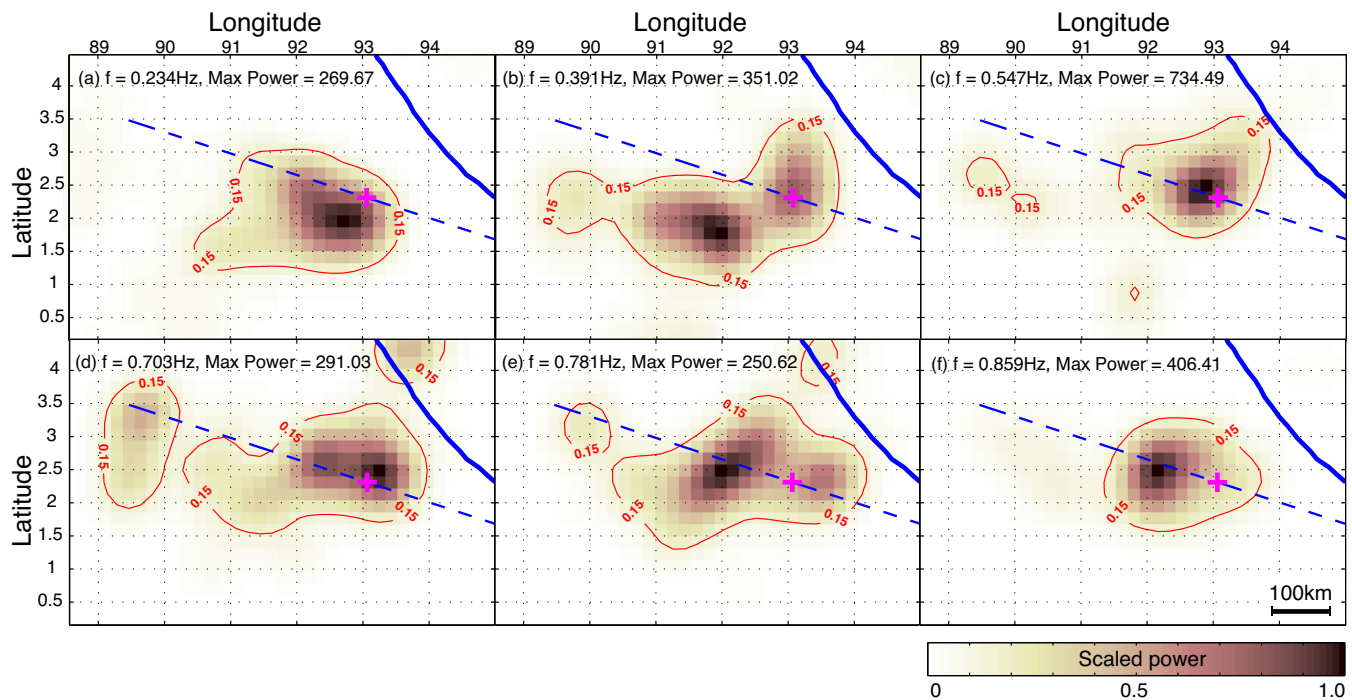

Figure 7. Coseismic radiation power distribution (background image) at each frequency as indicated. The power is normalized to its max power as given in each subplot.

distribution of the sources (seismic radiation) at 6 single frequencies (0.234, 0.391, 0.547, 0.703, 0.781 and 0.859 Hz) in Fig. 6 and the relative radiated power distribution of each frequency in Fig. 7. The length of the sliding window is set to be 10 s for the CS inversion.

In order to suppress artefacts that are generated during the CS inversion due to noise, we carefully examine the inversion results and only select the largest source obtained in each time window with good data fitting. Our results reveal complex rupture process
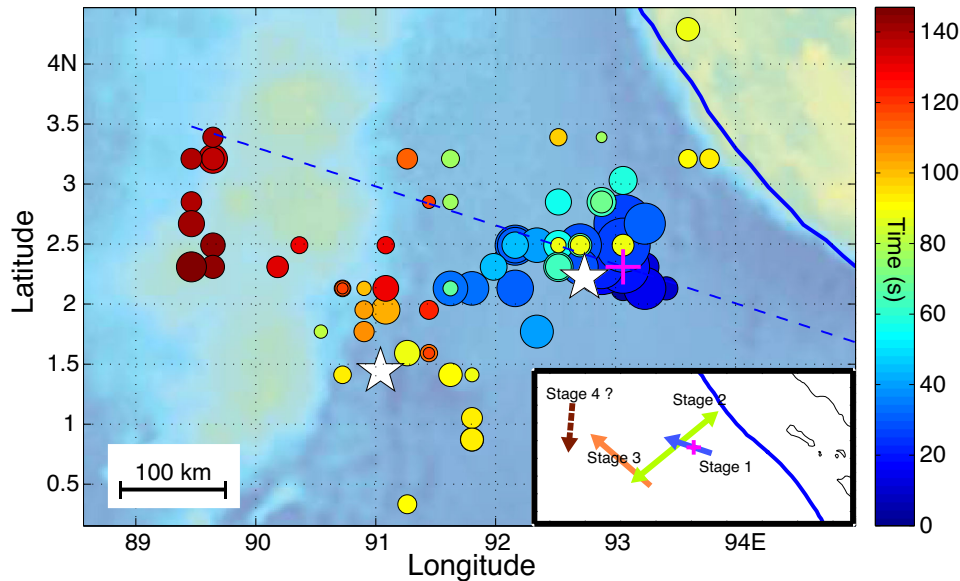
Figure 8. Seismic radiation in the frequency band 0.2–1 Hz. All results at different frequencies are summed up after Gaussian spatial smoothing (see eq. 12) and we only select the energy global maximum of each time snapshot indicated by the coloured circles. White stars indicate the positions of the best-fitting 2 point sources of the 2012 Sumatra M_w 8.6 event from Duputel *et al.* (2012). Other symbols are the same as previous figures.

concerning multiple faults and apparent frequency-dependence of seismic radiation during the main shock. At the lower frequencies (Figs 6 and 7a and b), regions with most energetic seismic radiation are located WSW of the epicentre. As frequency increases from about 0.5 to 0.8 Hz (Figs 6 and 7c and e), our results reveal more complex rupture processes: the energy radiation started around the epicentre area, then migrated bilaterally nearly perpendicular to the USGS strike direction (dashed blue line) after about 50 s and in the later stage marched towards and along the Ninety East Ridge (NER) after about 100 s. The highest energy radiation is around the epicentre area at 0.547 (Fig. 7c). At 0.859 Hz (Figs 6f and 7f), the highest seismic radiation appears about 100 km WNW of the epicentre.

4.2 Results in the frequency band 0.2–1 Hz

The M_w 8.6 strike-slip earthquake has a complex and large-scale rupture process as indicated by seismic radiation at various single frequencies. Here we will analyse the whole rupture process in a broader frequency band 0.2–1 Hz (Fig. 8) by summing up all single frequency results. The spatial distribution of seismic radiation is generally consistent with the aftershock distribution (see Fig. 1 yellow dots) except in the southernmost part where the aftershocks are probably related to the M_w 8.2 largest aftershock. This indicates a complicated rupture process and corresponds to a multi-fault rupture mode in this region. The whole rupture process can be mainly divided as 3 stages. First, in the first 50 s energy radiation started from the epicentre and the earthquake ruptured bilaterally towards WNW for about 100 km and towards ESE for about 50 km (called Stage 1, blue circles in Fig. 8). Then the energy radiation split and moved bilaterally towards both NE and SW directions for about 50 s (called Stage 2, green to yellow circles in Fig. 8). The rupture of Stage 2 took place on a fault that is almost orthogonal to the strike-slip fault of Stage 1, however, unparallel to the NNE-trending fracture zone. The northeastward-moving energy radiation reaches the Sumatra trench and may trigger an

event in the subduction zone at about 90 s (Figs 6d and 8), while the southwestward-marching radiation changed its direction and moved to a nearly perpendicular direction towards the NER between about 100 and 150 s (called Stage 3, orange to red circles in Fig. 8). In the last several tens of seconds, the seismic radiation also spread along the NER (around the latitude 89.5°). The focal mechanisms of large aftershocks around the NER region also show similar strike-slip mechanisms as the main shock and the M_w 8.2 aftershock, implying that the main shock has triggered a lot of seismicity on a series of ridge-perpendicular or ridge-parallel conjugate strike-slip faults.

4.3 Error estimation

We use a Monte Carlo error propagation method (Aster *et al.* 2013) to estimate the error of our L1–L1 norm based inversion. We add random Gaussian noise, which has amplitude of 10 per cent of the data amplitude and randomly shifted phase, to the data in frequency domain after filtering and then invert for the results. This procedure is repeated for 50 times and then we can get the spatial and amplitude distribution of results affected by random noise. Here we choose two time windows (12–22 s and 86–96 s) as examples, which have relatively strong signal (12–22 s, centred around 17 s, see Fig. 2) and relatively weak signal (86–96 s, centred around 91 s, see Fig. 2), respectively. All the obtained seismic sources from the Monte Carlo error propagation method are near the original position from the data without adding extra noise (see Fig. S4). Both the spatial distribution and amplitude of sources recovered from the CS inversion do not change much when relatively large random noise (10 per cent) is added to the data (Fig. S4). The results of error estimation indicate the stability of the inversion algorithm and its good resistance against random disturbance.

In order to examine the effect of noise level on the inversion results at different frequencies, we perform another Monte-Carlo error propagation tests. Different levels (from 5 to 50 per cent) of random Gaussian noise are added to the data in the time window

12–22 s at two different frequencies (0.234 and 0.547 Hz). For every noise level at each frequency, 50 tests are performed. The inversion results (source locations) are shown in Fig. S45. At the higher frequency (0.547 Hz), the inversion results (Fig. S5a) are quite robust even with noise level up to 50 per cent. However, at the lower frequency (0.234 Hz), large noise level (above ∼25 per cent) leads to much scattered source locations (Fig. S5b). This is mainly because the elements in the transmission matrix **A** (eq. 5) become more similar at lower frequencies, or the column vectors in **A** are more correlated with each other, thus resulting in the less stable inversion system given by eqs (7) or (8). Therefore, generally speaking, the inversion results at lower frequencies are more affected by the same level of noise in the data than at higher frequencies. However, at very high frequencies (e.g. above 1 Hz), the CS inversion results tends to appear unstable from our experiences, which is probably due to attenuation of earthquake signals and high noise levels.

5 DISCUSSION

5.1 Frequency-dependence of the rupture process

Frequency-dependence of earthquake rupture process has already been discussed in some previous studies. Yao *et al.* (2011, 2013) used the CS method to obtain the frequency-dependent rupture processes for four subduction zone megathrust earthquakes in the past 10 yr. Using the time-domain back-projection analyses, a few studies (Koper *et al.* 2011; Wang & Mori 2011; Lay *et al.* 2012) have similarly investigated frequency-dependent seismic radiation of subduction zone megathrust events, which is supposed to be caused by depth-varying frictional properties of subduction zone slab interfaces (Lay *et al.* 2012; Yao *et al.* 2013). For strike-slip events, Uchide *et al.* (2013) found that high frequency seismic radiation revealed by waveform backprojection typically originates at the margin of large slip patches that are obtained from slip inversion of relatively low frequency data.

Although the CS method using teleseismic *P* waves has nearly no vertical resolution, we compare our seismic radiation results with the slip inversion model from Wei *et al.* (2013). We find an approximate spatial correspondence between the large slip patches on the fault planes in their inversion and seismic energy radiation from the CS method on our predefined fault planes at the focal depth (22 km). Frequency-dependent rupture characteristics of this strike-slip event have been revealed by our results (Figs 6 and 7), particularly obvious in the first Stage 1 (about 0–50 s) of the rupture process. Because this event is a strike-slip event, we sum up the slip amount from Wei *et al.* (2013) along the depth direction to get the average slip along depth within different time windows for better comparison with our CS results (also see Fig. S6 for the slip distribution on each fault within different time windows). We take the summed energy radiation results from five continuous sliding windows (each window length is 10 s with a time step 2 s, overlapping by 8 s), corresponding to the waveforms within the 10–30 s window (see Fig. 2a) during the first stage (0–50 s), to analyse the frequency-dependent rupture process on the subfault 1 since it has the cleanest waveforms, which are not contaminated by the waveforms generated from other subfaults. Within the 10–30 s time window, the corrected source time (from eq. 11, shown in Figs 9a and b) is well consistent with the rupture time of each fault patch in the slip model. For the relatively lower frequency of 0.2–0.5 Hz (Fig. 9a), energy radiates from where large slip occurs on the fault. On the other hand, radiation from higher frequency of 0.5–1 Hz

(Fig. 9b) corresponds well to the boundary of large slip patches or rupture front (radiation with source time ∼26–33 s).

As revealed by some previous theoretical and numerical studies, seismic high-frequency waves are attributed to the abrupt changes of earthquake rupture velocity (Yamashita 1983) and the spectral amplitude of acceleration pulse depends linearly on the strain, the radius of the rupture front, the magnitude of the change in rupture velocity and the generalized radiation pattern coefficient (Sato 1994). In both sides of the slip boundary, there are abrupt changes of rupture properties, thus radiating energy with high-frequency components. Similar phenomenon has been observed in the event of 2010 EL Mayor-Cucapah, Mexico earthquake (Uchide *et al.* 2013).

We also check the results of Stage 2 and Stage 3, and can still observe the frequency-varying distribution of seismic radiation (e.g. within 60–90 s, Figs 9c and d and within 90–120 s, Figs 9e and f). However, unlike the results in Stage 1, the later stages are more complex and hard to be directly compared with slip inversion results due to several reasons. Firstly, as indicated by Lee *et al.* (2011) for the Tohoku M_w 9.0 earthquake, repeating slip can happen during great earthquake rupture processes. And this repetition is usually difficult to be resolved through the slip inversion method using low frequency waveform data and due to some model regularization assumptions in the slip inversion method. Our CS results (Figs 8 and 9) indicate that there may exist some repeating rupture during Stage 2, especially at the intersection region of subfaults 1 and 2 at about 60–70 s (Fig. 8) after the previous rupture front passed by. Secondly, the triggered events on some potential faults nearby can also be resolved by the CS inversion during the main shock rupture process. However, this also deteriorates the direct comparison with slip inversion results in the later stages. In the meanwhile, as for the Stage 3 the unclear fault structure in this region also brings difficulties for constraining the later rupture process, which leads to different settings of fault geometries in the finite fault inversion, for example in the last stage of this event presented by Yue *et al.* (2012) and Wei *et al.* (2013).

Since this event involves complex rupture modes of the multi-fault system in the Indian oceanic lithosphere, the variation of litho-spheric properties in the earthquake region may control the characteristics and extent of the rupture, and hence the spectral and spatial distribution of coseismic energy radiation. It was found that the spatial locations of coseismic rupture and aftershocks are strikingly confined in the regions with low gravity anomaly (Ishii *et al.* 2013), which may be caused by thinner oceanic crust or thermally modified lithosphere that is intrinsically weaker than the surrounding area. However, due to the lack of the structural information of the rupture area, it is still difficult to fully understand the detailed frequency-dependence rupture behaviour of this complex event.

5.2 Comparison with other results

We also use the conventional beamforming method to reconstruct the rupture process of this earthquake. The results (Fig. S7) are generally similar to the CS results (Fig. 8), however, appearing more concentrated than the CS results. Conventional beamforming results are relatively stable than the CS inversion method because it is based on stacking of the observed spectra (see eq. 12), and thus most of the uncorrelated components will be suppressed. However, as shown before (Figs 5 and S2), the CS method has higher spatial resolution without being greatly influenced by array configuration, and can also accurately separate multiple sources at lower frequencies than the beamforming method. As shown in Figs 6 and 8, the CS method
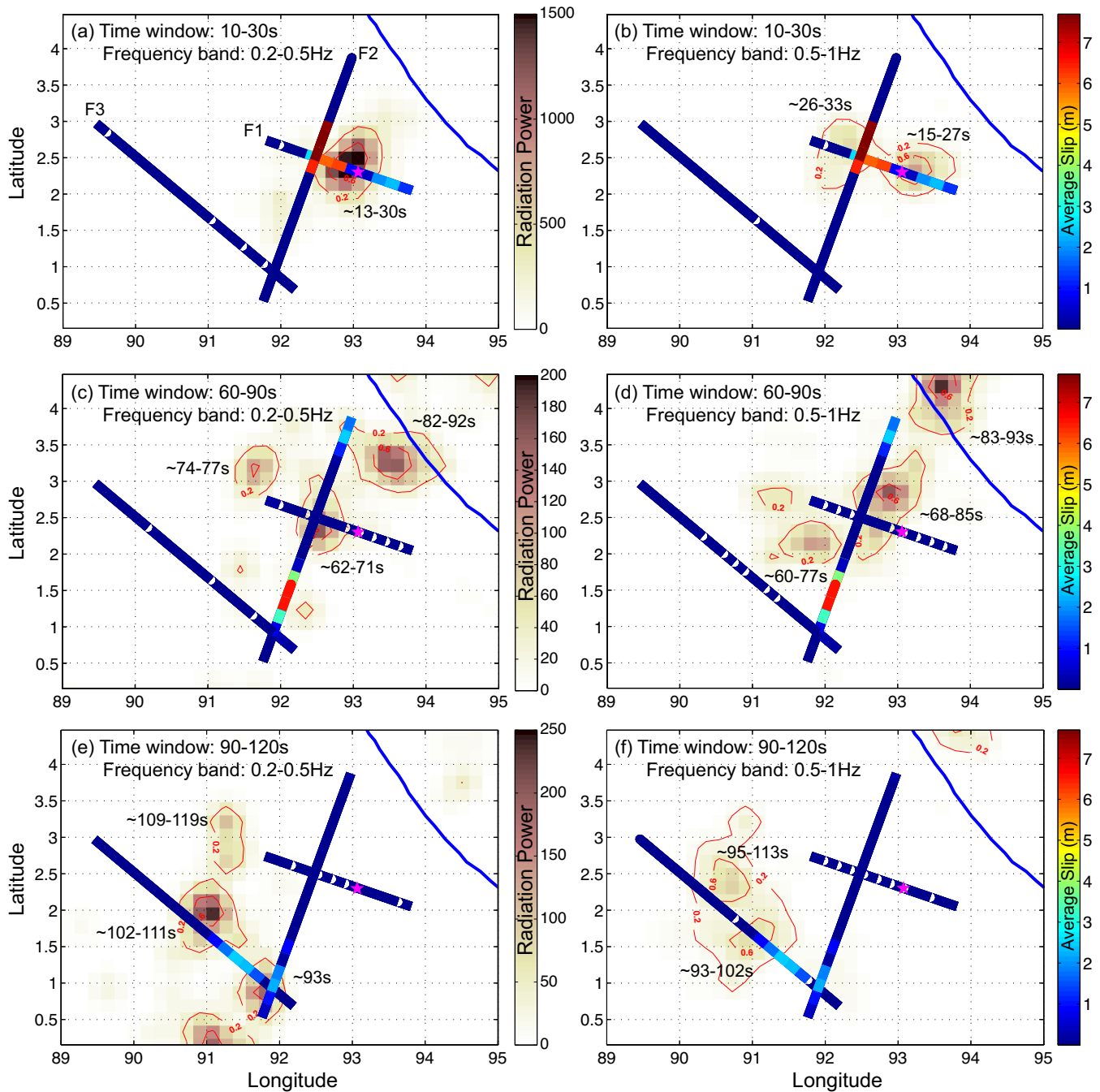
Figure 9. Comparison between average slip along the depth direction from the slip inversion model (coloured strips, from Wei *et al.* 2013) and coseismic radiation (background image) from three different time windows (10–30, 60–90 and 90–120 s, see Fig. 2 for waveforms) and within two different frequency bands (0.2–0.5 and 0.5–1 Hz) as indicated in each plot. Left and right colourbars are for the relative power of coseismic radiation and the average slip (m) along the depth direction within each time window, respectively. The numbers besides red contours denote the approximate energy radiation time. Other symbols are the same as those in the previous figures.

may generate some small scatters in the inversion results. However, as discussed in Section 5.1, some of the scatters are probably due to the triggering of small events on the nearby conjugate faults or repeating slip on the main faults, and a small portion of these scatters may be from the inversion of some inevitable data errors, especially some systematical data errors. How to better suppress the artefacts from systematical data errors, and make the CS method more stable and efficient is still a hot research topic in the CS community.

We compare our results from the CS method with those from other backprojection methods (Meng *et al.* 2012; Satriano *et al.* 2012; Wang *et al.* 2012; Ishii *et al.* 2013) and from the slip inversion method (Yue *et al.* 2012; Wei *et al.* 2013). The results of this great earthquake from different methods all share a complex, multi-fault rupture process. Our results also share some similarities as the multipoint-source inversion results (Duputel *et al.* 2012) (see white stars in Fig. 8). Most results give a complex multi-stage rupture process on a series of conjugate strike-slip faults: first

stage along the WNW–ESE direction, then second stage splitting to almost orthogonally NNE–SSW direction, and finally the third stage turning again towards NW until reaching the NER. However, Satriano *et al.* (2012) propose that the complicated westward rupture process may be related to dynamic triggering of the pre-existing NNE-trending faults (fracture zones) due to early generated surface waves. Whether dynamic triggering of multiple nearly parallel faults is a possible mechanism for this event needs further rupture dynamics simulation.

The finite fault slip model of Yue *et al.* (2012) consists of four subfaults, while Wei *et al.* (2013) use three subfaults in their slip inversion based on the backprojection results from Meng *et al.* (2012). Results from both of them share similar features except some differences on assumptions before slip inversion and the final slip magnitude. The most dominant differences between these two slip models are the fault settings in the last stage of this event: in the model of Wei *et al.* (2013), the final rupture process is set on a SE-NW fault extending as long as 400 km, while Yue *et al.* (2012) choose the relatively complex fault settings with 2 parallel/conjugate subfaults. The overall coseismic radiation patterns from backprojection (Meng *et al.* 2012; Satriano *et al.* 2012; Wang *et al.* 2012; Ishii *et al.* 2013) and our CS method (Figs 6–8) are well compatible with both the slip models except some details in the last rupture stage due to different model settings. The changes of rupture behaviour during the main shock, which lead to the frequency-varying coseismic radiation resolved by the CS method, are related to changes in physical properties in the source region, for instance, 3-D fault geometry, frictional properties on the fault surface, accumulated tectonic stresses, etc. These information will be important for understanding earthquake mechanisms as well as future seismic hazards in this region.

6 CONCLUSIONS

We use the CS inversion method to invert for the rupture process and frequency-dependent seismic radiation of the 2012 April 11 M_w 8.6 Sumatra great strike-slip earthquake. A series of synthetic tests are designed to assure the robustness and resolution of the proposed L1–L1 norm CS inversion method. These tests indicate high spatial resolution and great resistance against data outliers of our method. The inversion results show a complex multistage rupture process for this great earthquake. The rupture involves at least three nearly conjugate strike-slip faults in the oceanic lithosphere between the Sumatra trench and Ninety East Ridge. The main shock has triggered a lot of events on a series of ridge-perpendicular or ridge-parallel conjugate strike-slip faults around the Nighty East Ridge. Compared with slip model, some lower frequency radiation appears to originate from the areas with large slip, while some high-frequency radiation is located at the boundary of large-slip region or rupture front. Some seismic radiation probably originates from the repeating slip on the main faults or triggered events on some nearby faults in the rupture area. Although the lack of structural information limits our understanding of detailed frequency-dependent rupture behaviour of this event, our results provide interesting observations for further investigation of rupture physics of this complex strike-slip event in the future.

ACKNOWLEDGEMENTS

REFERENCES

Aster, R.C., Borchers, B. & Thurber, C.H., 2013. *Parameter Estimation and Inverse Problems,* Academic Press.

Bouchon, M. & Vallée, M., 2003. Observation of long supershear rupture during the magnitude 8.1 Kunlunshan earthquake, *Science,* **301,** 824–826.

Bouchon, M., Bouin, M.P., Karabulut, H., Toksöz, M.N., Dietrich, M. & Rosakis, A.J., 2001. How fast is rupture during an earthquake? New insights from the 1999 Turkey earthquakes, *Geophys. Res. Lett.,* **28,** 2723–2726.

Boyd, S. & Vandenberghe, L., 2004. *Convex Optimization,* Cambridge Univ. Press.

Candes, E.J., Romberg, J.K. & Tao, T., 2006. Stable signal recovery from incomplete and inaccurate measurements, *Commun. Pure Appl. Math.,* **59,** 1207–1223.

Capon, J., 1969. High-resolution frequency-wavenumber spectrum analysis, *Proc. IEEE.,* **57,** 1408–1418.

Donoho, D.L., 2006. Compressed sensing, *IEEE T. Inform. Theory.* **52,** 1289–1306.

Duputel, Z., Kanamori, H., Tsai, V.C., Rivera, L., Meng, L., Ampuero, J.-P. & Stock, J.M., 2012. The 2012 Sumatra great earthquake sequence, *Earth planet. Sci. Lett.,* **351–352,** 247–257.

Hayes, G.P., Furlong, K.P. & Ammon, C.J., 2009. Intraplate deformation adjacent to the Macquarie Ridge south of New Zealand—the tectonic evolution of a complex plate boundary, *Tectonophysics,* **463,** 1–14.

Ishii, M., Shearer, P.M., Houston, H. & Vidale, J.E., 2005. Extent, duration and speed of the 2004 Sumatra–Andaman earthquake imaged by the Hi-Net array, *Nature,* **435,** 933–936.

Ishii, M., Kiser, E. & Geist, E.L., 2013. M_w 8.6 Sumatran earthquake of 11 April 2012: rare seaward expression of oblique subduction, *Geology,* **41,** 319–322.

Kennett, B.L.N. & Engdahl, E.R., 1991. Traveltimes for global earthquake location and phase identification, *Geophys. J. Int.,* **105,** 429–465.

Koper, K.D., Hutko, A.R., Lay, T., Ammon, C.J. & Kanamori, H., 2011. Frequency-dependent rupture process of the 11 March 2011 M_w 9.0 Tohoku earthquake: comparison of short-period *P* wave backprojection images and broadband seismic rupture models, *Earth Planets Space,* **63,** 599–602.

Lay, T., Kanamori, H., Ammon, C.J., Koper, K.D., Hutko, A.R., Ye, L., Yue, H. & Rushing, T.M., 2012. Depth-varying rupture properties of subduction zone megathrust faults, *J. geophys. Res.,* **117,** B04311, doi:10.1029/2011JB009133.

Lee, S.J., Huang, B.S., Ando, M., Chiu, H.C. & Wang, J.H., 2011. Evidence of large scale repeating slip during the 2011 Tohoku-Oki earthquake, *Geophys. Res. Lett.,* **38,** doi:10.1029/2011GL049580.

Malioutov, D., Çetin, M. & Willsky, A.S., 2005. A sparse signal reconstruction perspective for source localization with sensor arrays, *IEEE T. Signal. Process.,* **53,** 3010–3022.

Meng, L., Inbal, A. & Ampuero, J.-P., 2011. A window into the complexity of the dynamic rupture of the 2011 M_w 9 Tohoku-Oki earthquake, *Geophys. Res. Lett.,* **38,** L00G07, doi:10.1029/2011GL048118.

Meng, L., Ampuero, J.P., Stock, J., Duputel, Z., Luo, Y. & Tsai, V.C., 2012. Earthquake in a maze: compressional rupture branching during the 2012 M(w) 8.6 Sumatra earthquake, *Science,* **337,** 724–726.

Obara, K., Kasahara, K., Hori, S. & Okada, Y., 2005. A densely distributed high-sensitivity seismograph network in Japan: Hi-net by National Research Institute for Earth Science and Disaster Prevention, *Rev. Sci. Instrum.,* **76,** 021301, doi:10.1063/1.1854197.

Pollitz, F.F., Stein, R.S., Sevilgen, V. & Burgmann, R., 2012. The 11 April 2012 east Indian Ocean earthquake triggered large aftershocks worldwide, *Nature,* **490,** 250–253.

Rost, S., 2002. Array seismology: methods and applications, *Rev. Geophys.,* **40,** 1008, doi:10.1029/2000RG000100.

Sato, T., 1994. Seismic radiation from circular cracks growing at variable rupture velocity, *Bull. seism. Soc. Am.,* **84,** 1199–1215.

Satriano, C., Kiraly, E., Bernard, P. & Vilotte, J.-P., 2012. The 2012 M_w 8.6 Sumatra earthquake: evidence of westward sequential seismic ruptures associated to the reactivation of a N-S ocean fabric, *Geophys. Res. Lett.,* **39,** L15302, doi:10.1029/2012GL052387.

Schmidt, R.O., 1986. Multiple emitter location and signal parameter estimation, *IEEE Trans. Antenn. Propag.,* **34,** 276–280.

Simons, M. *et al.*, 2011. The 2011 magnitude 9.0 Tohoku-Oki earthquake: mosaicking the megathrust from seconds to centuries, *Science,* **332,** 1421–1425.

Spudich, P. & Frazer, L.N., 1984. Use of ray theory to calculate high-frequency radiation from earthquake sources having spatially variable rupture velocity and stress drop, *Bull. seism. Soc. Am.,* **74,** 2061–2082.

Tocheport, A., Rivera, L. & Van der Woerd, J., 2006. A study of the 14 November 2001 Kokoxili Earthquake: history and geometry of the rupture from teleseismic data and field observations, *Bull. seism. Soc. Am.,* **96,** 1729–1741.

Tsuboi, S., Komatitsch, D., Ji, C. & Tromp, J., 2003. Broadband modeling of the 2002 Denali fault earthquake on the Earth Simulator, *Phys. Earth. planet. Int.,* **139,** 305–313.

Uchide, T., Yao, H. & Shearer, P.M., 2013. Spatio-temporal distribution of fault slip and high-frequency radiation of the 2010 El Mayor-Cucapah, Mexico earthquake, *J. geophys. Res.: Solid Earth,* **118,** 1546–1555.

VanDecar, J. & Crosson, R., 1990. Determination of teleseismic relative phase arrival times using multi-channel cross-correlation and least squares, *Bull. seism. Soc. Am.,* **80,** 150–169.

Walker, K.T. & Shearer, P.M., 2009. Illuminating the near-sonic rupture velocities of the intracontinental Kokoxili M_w 7.8 and Denali fault M_w 7.9 strike-slip earthquakes with global *P* wave back projection imaging, *J. Geophys. Res.,* **114,** B02304, doi:10.1029/2008JB005738.

Wang, D. & Mori, J., 2011. Frequency-dependent energy radiation and fault coupling for the 2010 M_w 8.8 Maule, Chile, and 2011 M_w 9.0 Tohoku, Japan, earthquakes, *Geophys. Res. Lett.,* **38,** L22308, doi:10.1029/2011GL049652.

Wang, D., Mori, J. & Uchide, T., 2012. Supershear rupture on multiple faults for the M_w 8.6 Off Northern Sumatra, Indonesia earthquake of April 11, 2012, *Geophys. Res. Lett.,* **39,** L21307, doi:10.1029/2012GL053622.

Wei, S., Helmberger, D. & Avouac, J.-P., 2013. Modeling the 2012 Wharton basin earthquakes off-Sumatra: complete lithospheric failure, *J. geophys. Res.: Solid Earth,* **118,** 3592–3609.

Yamashita, T., 1983. High-frequency acceleration radiated by unsteadily propagating cracks and its near-source geometrical attenuation, *J. Phys. Earth.,* **31,** 1–32.

Yang, J. & Zhang, Y., 2011. Alternating direction algorithms for L1-problems in compressive sensing, *SIAM J. Sci. Comput.,* **33,** 250–278.

Yao, H., Gerstoft, P., Shearer, P.M. & Mecklenbräuker, C., 2011. Compressive sensing of the Tohoku-Oki M_w 9.0 earthquake: Frequency-dependent rupture modes, *Geophys. Res. Lett.,* **38,** L20310, doi:10.1029/2011GL049223.

Yao, H., Shearer, P.M. & Gerstoft, P., 2013. Compressive sensing of frequency-dependent seismic radiation from subduction zone megathrust ruptures, *Proc. Natl. Acad. Sci. U.S.A.,* **110,** 4512–4517.

Yue, H., Lay, T. & Koper, K.D., 2012. En echelon and orthogonal fault ruptures of the 11 April 2012 great intraplate earthquakes, *Nature,* **490,** 245–249.

SUPPORTING INFORMATION

Additional Supporting Information may be found in the online version of this paper:

Figure S1. Waveforms and stations selection process. (a) Waveforms recorded at all the selected Hi-net stations. (b) Zoom-in of the first 8s waveforms, which are used to do the cross-correlation. (c) Cross-correlation coefficient distribution of each station. Blue dashed line shows the cross-correlation coefficient threshold (0.7) used in this study. (d) Distribution of all the 567 Hi-net stations (blue triangles). There are total 275 stations satisfying this threshold with their waveforms shown in Fig. 2 and station distribution shown in Fig. 3 in the main text.

Figure S2. Synthetic tests for two different seismic array distributions. (a) and (b) are the CS and beamforming results, respectively, for the station distribution shown in (c). (d) and (e) are the CS and beamforming results, respectively, for the station distribution shown in (f). Black arrows are pointing to the direction of seismic array. Other symbols are the same as those in the Fig. 4.

Figure S3. Synthetic tests indicating the influence from stations resampling. (a) Results from the CS method using all the stations [red triangles in (d) and (e)]. (b) Results from the CS method using 30 per cent randomly selected stations [blue triangles in (d)]. (c) Results from CS method using part of all stations [blue triangles in (e)]. Other symbols are the same as those in Fig. 4.

Figure S4. Error analysis of the CS results at $f = 0.547$ Hz using the Monte Carlo (MC) error propagation method with 10 per cent random noise added. (a) Spatial distribution of 50 MC estimation of the source locations (blue crosses) for the 12–22 s time window. (b) Source amplitudes (*y*-axis) recovered from 50 MC estimations (blue crosses) for the 12–22 s time window. Red *X* and dashed line represent the results from CS without extra random noise. (c) and (d) are the same as (a) and (b) except for the 86–96 s time window.

Figure S5. Monte-Carlo error propagation tests for the 12–22 s time window at (a) 0.547 Hz and (b) 0.234 Hz. For the test, we add random noise to the data and perform the inversion. For each noise level (ratio of noise to signal amplitude) shown as the number beside the coloured crosses on the right, we repeat inversion for 50 times and all results are plotted as the crosses with the corresponding noise-level colour in (a) and (b). The black $+$ is the original source position.

Figure S6. Slip inversion results from (a) subfault 1; (b) subfault 2; (c) subfault 3 in Wei *et al*. (2013). Only the slip within 10–30 s, 60–90 s and 90–120 s time windows are shown, corresponding to the depth-averaged slip in Fig. 9. White contours indicate the time (s) as labelled.

Figure S7. Seismic radiation in the frequency band 0.2–1 Hz using the beamforming method. For the meaning of symbols, please refer to Fig. 8.

(http://gji.oxfordjournals.org/lookup/suppl/doi:10.1093/gji/ggw105/-/DC1)

Please note: Oxford University Press is not responsible for the content or functionality of any supporting materials supplied by the authors. Any queries (other than missing material) should be directed to the corresponding author for the paper.